


# Effect of Anodization on the Stress Corrosion Cracking Behavior of The AZ61 Magnesium Alloy in 0.1 M NaCl Solution

Fábio Okamoto<sup>a</sup> , Mara Cristina Lopes de Oliveira<sup>a</sup> , Adenilson Almeida Silva<sup>b</sup>,  
Roosevelt Droppa Jr<sup>a</sup>, Renato Altobelli Antunes<sup>a,\*</sup> 

<sup>a</sup>Universidade Federal do ABC (UFABC), Centro de Engenharia, Modelagem e Ciências Sociais Aplicadas (CECS), 09210-580, Santo André, SP, Brasil.

<sup>b</sup>Instituto de Pesquisas Energéticas e Nucleares (IPEN/CNEN-SP), Centro de Células a Combustível e Hidrogênio, Av. Prof. Lineu Prestes, 2242, Cidade Universitária, 05508-000, São Paulo, SP, Brasil.

Received: August 08, 2022; Revised: March 06, 2023; Accepted: March 23, 2023

In the present work, the AZ61 alloy, one of the most important commercial structural magnesium alloys, was anodized in three different alkaline electrolytes consisting of 3 M KOH + 0.15 M Na<sub>2</sub>SiO<sub>3</sub> + 0.1 M Na<sub>2</sub>B<sub>4</sub>O<sub>7</sub>·10H<sub>2</sub>O, 3 M KOH + 0.5 M Na<sub>3</sub>PO<sub>4</sub> and 3 M KOH + 0.50 M Na<sub>2</sub>SiO<sub>3</sub>. The treatment was conducted at two different current densities, 20 and 30 mA·cm<sup>-2</sup> for 10 minutes. The anodized layers were characterized by scanning electron microscopy, X-ray diffractometry and X-ray photoelectron spectroscopy. The corrosion resistance was assessed by potentiodynamic polarization tests. The SCC behavior was studied using slow strain rate tests in 0.1 M NaCl solution at room temperature. Conventional tensile tests were also conducted in air. The susceptibility to SCC was dependent on the morphology of the anodized film. The composition of the electrolyte and the current density of the anodization treatment affected the SCC susceptibility of the AZ61 alloy. The best corrosion resistance and the lowest susceptibility to SCC were obtained for samples anodized in the borate-containing electrolyte at 30 mA·cm<sup>-2</sup>. The smooth and compact surface morphology of the anodized film obtained in this condition was the main reason for the improved SCC behavior of the AZ61 alloy.

**Keywords:** stress corrosion cracking, AZ61, magnesium alloy, anodization.

## 1. Introduction

Lightweight metallic alloys are attractive for saving weight and reducing fuel consumption in the automotive and aerospace industries<sup>1</sup>. Magnesium alloys play a central role in this scenario due to their well-known low density and high strength-to-weight ratio<sup>2,3</sup>. One major limitation for expanding their applications is the low corrosion resistance in the atmosphere and chloride-containing aqueous solutions<sup>4,5</sup>. The naturally formed surface oxide film, mainly consisting of Mg(OH)<sub>2</sub>, has limited protection ability in these environments<sup>6,7</sup>.

Corrosion protection methods are, therefore, a must-attend issue for expanding the engineering applications of magnesium and its alloys. For practical purposes, anodization has been widely employed to form protective oxide layers on these materials<sup>8-10</sup>. Typically, alkaline electrolytes are employed to produce stable oxide growth during the electrolytic treatment of the magnesium substrate<sup>11,12</sup>. Silicate-based solutions are frequently reported as a viable route to carry out the anodization process in an environmentally friendly electrolyte<sup>13,14</sup>. As proposed by Fukuda and Matsumoto<sup>15</sup>, a mixed Mg<sub>2</sub>SiO<sub>4</sub> and SiO<sub>2</sub> surface film would be formed. Other electrolytes containing phosphate and borate ions have also been reported in the literature<sup>16,17</sup>.

As one of the most widely used structural lightweight materials, aluminum-containing magnesium alloys, especially, the AZ series, concentrate much research interest for developing effective surface treatments to withstand corrosion<sup>18,19</sup>. One additional concern for load-bearing components made of magnesium alloys is related to their intrinsic susceptibility to stress corrosion cracking (SCC) in chloride-containing environments and even in distilled water<sup>20-22</sup>. According to Cao et al.<sup>23</sup>, localized corrosion spots may be preferential sites for the initiation of SCC. In this regard, the presence of a surface film, such as the oxide layer formed by anodization, may affect the SCC behavior of magnesium alloys. In fact, surface oxide films may act as stress risers, increasing the susceptibility of magnesium alloys to corrosion-assisted mechanical failures, such as SCC and corrosion-fatigue<sup>24,25</sup>. In the literature, there is scarce information on the influence of anodizing parameters such as electrolyte composition and current density on the SCC behavior of magnesium alloys. Although this topic is of great scientific and technological interest to expand the applicability of magnesium alloys, it still remains little explored. For example, Srinivasan et al.<sup>24,26</sup> have studied the effect of an oxide layer obtained by plasma electrolytic oxidation on the SCC behavior of the AM50 (Mg-Al-Mn) alloy. They observed only a marginal decrease of the SCC susceptibility due to the presence of the protective coating.

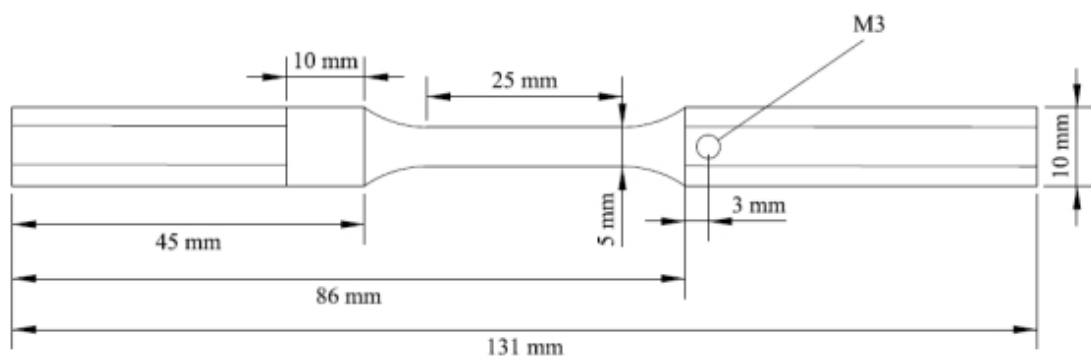
\*e-mail: [renato.antunes@ufabc.edu.br](mailto:renato.antunes@ufabc.edu.br)

**Table 1.** Nominal chemical composition of the AZ61 alloy<sup>26</sup>.

	Al	Cu	Fe	Mn	Ni	Si	Zn	Mg
mass (%)	5.8 – 7.2	<0,05	<0.005	0.15 – 0.5	<0.005	0.10	0.4 – 1.5	Bal.

**Table 2.** Anodization parameters and sample designation.

Electrolyte	Current density (mA.cm <sup>-2</sup> )	Time (min)	pH	Sample identification
3 M KOH + 0.5 M Na <sub>3</sub> PO <sub>4</sub>	20	10	13.63	PHO-20
	30	10		PHO-30
3 M KOH + 0.5 M Na <sub>2</sub> SiO <sub>3</sub>	20	10	13.70	SI-20
	30	10		SI-30
3 M KOH + 0.15 M Na <sub>2</sub> SiO <sub>3</sub> + 0.1 M Na <sub>2</sub> B <sub>4</sub> O <sub>7</sub> ·10H <sub>2</sub> O	20	10	13.63	BO-20
	30	10		BO-30

**Figure 1.** Schematic drawing of the SSRT specimens.

Similar findings were also encountered by the same research group for plasma electrolytic oxidation treated AZ61 alloy<sup>27</sup>. However, the effect of electrolyte composition and electrical parameters of the electrolytic treatment were not assessed. Furthermore, thorough assessment of the correlation between coating composition and the SCC behavior of the Mg alloys was not provided. This information is relevant to widen the structural applications of the AZ61 alloy in the anodized condition, but it is still lacking in the literature.

In the light of scenario depicted above, the aim of the present work was to investigate the influence of the electrolyte composition and the current density of the anodization process on the SCC behavior of the AZ61 magnesium alloy in sodium chloride solution at room temperature. Slow strain rate tests (SSRT) were employed with this purpose. The correlation between composition, morphology and structure of the anodized film with the SCC behavior of the AZ61 alloy is also discussed.

## 2. Experimental

### 2.1. Material and specimen preparation

The AZ61 alloy used in this work (nominal chemical composition shown in Table 1) was purchased from Xi'an Yuechen Metal Products Co, Ltd (China) in the form of extruded bars with circular cross-section (28 mm diameter).

Specimens for the electrochemical tests were cut from the as-received AZ61 bars using silicon carbide blades in a cut-off machine, thus obtaining round discs with a thickness of 3 mm. Surface finishing was comprised of grinding with silicon carbide waterproof sandpapers up to #2000 grit. After grinding, the specimens were rinsed with ethanol and thoroughly washed with distilled water.

Specimens for the SSRT tests were prepared using a CNC machine (Romi D600). A schematic drawing of the machined specimens is displayed in Figure 1. The dimensions (mm) were based on the ASTM B107/B107M, ASTM B557 and ASTM E8/E8M standards<sup>28-30</sup>. After machining, surface finishing was comprised of grinding with silicon carbide waterproof sandpapers up to grit #2000, rinsed with ethanol and distilled water.

### 2.2. Anodization

Anodization was carried out under current controlled condition for 10 minutes at room temperature. The solution was magnetically stirred to ensure homogeneous temperature. Three different electrolytes and two different current densities were employed, as shown in Table 2. Sample designation is also displayed in this table.

A direct current source power supply (Maisen MP5003D) was employed for conducting the anodizing treatment.

A stainless steel container was used as the cell and also as the cathode for the electrolytic process. The electrolyte volume in the cell was 1.0 L.

### 2.3. Morphology, structure and composition of the anodized layer

The morphology and chemical composition of the anodized layer was examined using scanning electron microscopy (Leica/LEO 440i) coupled to an energy dispersive X-ray spectrometer (EDS). X-ray diffractometry was employed to assess the crystalline phases of the anodic films, using a Bruker Discover D8 instrument equipped with Cu- $\alpha$  anode. The measurements were made at a glancing angle of  $0.75^\circ$ . Surface roughness was measured using a confocal laser scanning microscope (Olympus LEXT OLS4100).

The surface chemistry of the anodized layers was examined by XPS using a Thermo VG K-alpha+ spectrometer operating with Al-K $\alpha$  radiation source. The pressure in the analysis chamber was  $10^{-7}$  Pa. The spot size was  $400 \mu\text{m}$ . Peak fitting was carried out by subtracting the background with the Smart© algorithm in the Advantage software. The binding energy scale was calibrated with respect to the adventitious carbon peak at 284.8 eV.

### 2.4. Electrochemical tests

Electrochemical measurements were conducted with a M101 Autolab potentiostat/galvanostat in a conventional three-electrode cell configuration. A platinum wire was used as counter-electrode, Ag/AgCl (KCl, 3 M) was the reference electrode and the AZ61 samples were the working electrodes. The tests were conducted in 0.1 M NaCl solution at room temperature. Initially, the open circuit potential was monitored for 60 minutes. Next, the samples were subject to potentiodynamic polarization in the potential range of  $-300$  mV versus the OCP up to  $0 \text{ V}_{\text{Ag/AgCl}}$  at a sweep rate of  $1 \text{ mV}\cdot\text{s}^{-1}$ . To ensure reproducibility at least three specimens were tested.

### 2.5. Slow strain rate tensile tests

SSRT tests were conducted in 0.1 M NaCl at room temperature. The specimens were subject to uniaxial tensile tests at a deformation rate of  $10^{-6} \text{ s}^{-1}$  in a universal testing machine (MTS, Exceed 45), according to the ASTM G129 standard<sup>31</sup>. The machine was equipped with a homemade acrylic cell to hold the electrolyte, as schematically shown in Figure 2. The tests were conducted in triplicate. The elongation (EL) at break and ultimate tensile strength (UTS) of the specimens were determined from the engineering stress-strain curves. The tests were also conducted in air for comparison. After failure, the fracture surfaces were cleaned in  $10 \text{ g L}^{-1} \text{ CrO}_3$  solution at room temperature for 5 minutes, according to ASTM G1-90 to remove the corrosion products. Next, after rinsing in deionized water and drying in a warm air stream, fractographic analysis was carried out in a Leica/LEO 440i scanning electron microscope.

Susceptibility indices  $I_{\text{SCC}}$  and  $I_\epsilon$  were calculated based on Equations 1 and 2, respectively, where  $\epsilon$  is the elongation at break. Values close to unity indicate high susceptibility to SCC, whereas the opposite takes place for values close to zero<sup>32,33</sup>.

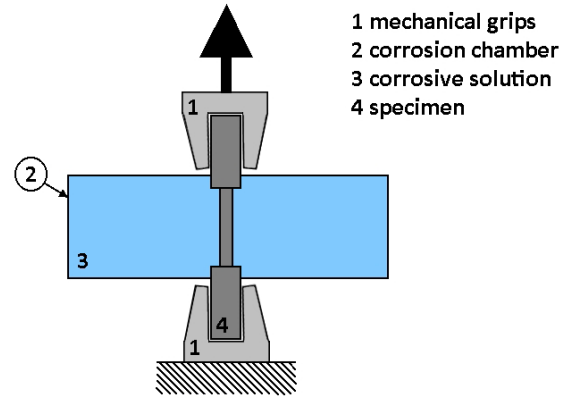


Figure 2. Schematic representation of the SSRT set up.

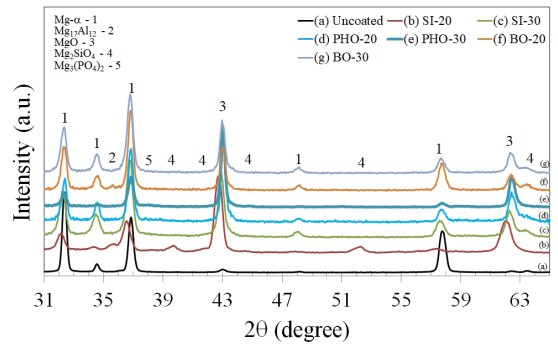


Figure 3. XRD patterns of the uncoated and anodized AZ61 alloy.

$$I_{\text{SCC}} = \frac{UTS_{\text{air}} - UTS_{\text{NaCl}}}{UTS_{\text{air}}} \quad (1)$$

$$I_\epsilon = \frac{\epsilon_{\text{air}} - \epsilon_{\text{NaCl}}}{\epsilon_{\text{air}}} \quad (2)$$

## 3. Results and Discussion

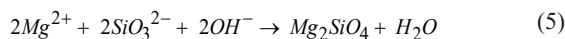
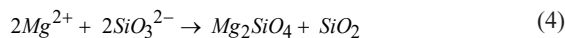
### 3.1. Structure, morphology and composition of the anodized layers

#### 3.1.1. X-ray diffraction analysis

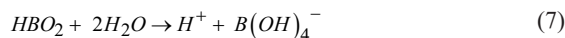
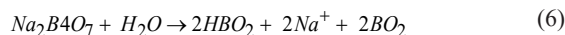
The crystalline phases formed on the anodized layers were identified by X-ray diffractometry. Figure 3 displays the XRD patterns of the as-received and anodized AZ61 alloy. The Mg- $\alpha$  and Mg<sub>17</sub>Al<sub>12</sub> peaks originated from the AZ61 alloy substrate are clearly seen for all samples. The main phase in the anodized films is MgO. According to Bai and Chen<sup>34</sup>, MgO forms by the migration of Mg<sup>2+</sup> ions from the substrate to the film/electrolyte interface, and also by the migration of O<sup>2-</sup> from the electrolyte to the substrate/film interface, following reaction (3).



In addition to MgO, Mg<sub>2</sub>SiO<sub>4</sub> peaks were also observed in the XRD patterns of the samples anodized in the silicate and borate-based electrolytes. This phase is frequently reported for anodized layers obtained in silicate-based electrolytes<sup>35,36</sup>. The formation of Mg<sub>2</sub>SiO<sub>4</sub> proceeds according to Equations 4 and 5<sup>15</sup>.



Borate phases were not identified in the anodized layers formed on the 3 M KOH + 0.15 M Na<sub>2</sub>SiO<sub>3</sub> + 0.1 M Na<sub>2</sub>B<sub>4</sub>O<sub>7</sub>·10H<sub>2</sub>O solution, as also reported by other authors<sup>37-39</sup> for anodic films formed on magnesium alloys in borate-containing electrolytes. Zhang et al.<sup>40</sup>, in turn, reported boron incorporation into the anodic film obtained by plasma electrolytic oxidation of the AZ91D alloy. However, the sodium borate concentration in the electrolyte was higher than that used in the present work. The role of sodium borate, even when boron compounds are not present in the anodic film, may be important to thickness and porosity control, thus affecting the corrosion properties of the anodized layer. As described by Zhang et al.<sup>40</sup>, sodium borate influences the electrolyte conductivity. Hence, it affects the sparks generated during the oxidation treatment, likely influencing the formation of a more homogeneous and compact oxide layer on the metallic substrate. According to these authors, when sodium borate is added to the electrolyte, its dissolution occurs as shown in Equation 6. HBO<sub>2</sub> is a weak acid and H<sup>+</sup> ions may form, according to Equation 7.



The base electrolyte (3 M KOH solution) is strongly alkaline (pH = 13.63, as shown in Table 2) and its OH<sup>-</sup> ions may react with the H<sup>+</sup> dissociated from HBO<sub>2</sub>, thus producing water. As a consequence, electrolyte conductivity is decreased due to the lower conductivity of the water molecules with respect to OH<sup>-</sup> ions. Hence, sparks becomes less intense, thus leading to a thinner, less defective oxide layer.

In the phosphate-based electrolyte the dominant crystalline phase is also MgO, as also displayed in Figure 3. Peaks from the substrate were also observed (Mg-*α* and Mg<sub>17</sub>-Al<sub>12</sub>). In addition to MgO, a weak magnesium phosphate (Mg<sub>3</sub>(PO<sub>4</sub>)<sub>2</sub>) peak was observed at 37.8°. This phase is also reported in the literature in the oxide film obtained from electrolytic oxidation processes of magnesium alloys in sodium phosphate-based electrolytes<sup>41,42</sup>.

### 3.1.2. Surface and cross-section morphologies

Figure 4 shows SEM micrographs of the top surfaces of the anodized layers. The films obtained in the 3 M KOH + 0.5 M Na<sub>2</sub>SiO<sub>3</sub> electrolyte display pores and cracks that are typically formed during anodization of magnesium alloys<sup>43,44</sup>. The morphological features of the SI-20 (Figure 4a) and SI-30 (Figure 4b) samples are nearly the same, suggesting the increase of the anodizing current density did not change the surface topography of the anodic film. EDS maps (Supplementary Files – Figures S1 and S2) confirm that

Mg and Si are spread over the whole surface, being the major part of the anodized layers formed on SI-20 and SI-30 samples.

The films obtained in the 3 M KOH + 0.5 M Na<sub>3</sub>PO<sub>4</sub>, in turn, display a distinct surface aspect. As seen in Figure 4c, the anodized layer formed on the PHO-20 sample exhibits a duplex character. Part of the surface displays a rough topography permeated by pores and cracks, whereas other regions are smoother (central region of Figure 4c). EDS mapping (Supplementary File – Figure S3) revealed that the smooth region does not contain phosphorus, being the magnesium signal much more intense at this site than at the rougher peripheral sites. The same features were observed for the PHO-30 sample (Figure 4d and Figure S4 – Supplementary File), with the difference that the smooth area is smaller than for PHO-20, suggesting the phosphate-rich anodized layer have grown faster when the current density increased from 20 to 30 mA·cm<sup>-2</sup>. In fact, the applied current density may trigger the growth of the anodized layer, as reported by Chai et al.<sup>45</sup>.

When anodization was carried out in the 3 M KOH + 0.15 M Na<sub>2</sub>SiO<sub>3</sub> + 0.1 M Na<sub>2</sub>B<sub>4</sub>O<sub>7</sub>·10H<sub>2</sub>O electrolyte, the surface aspect became smoother. As seen in Figure 4e, the BO-20 layer covers the whole surface and displays fewer pores and cracks when compared to the SI-20 (Figure 4a) and PHO-20 (Figure 4c) anodic films. The topography became even more compact for the BO-30 sample (Figure 4f). EDS maps reveal that magnesium is evenly distributed on the anodic films of these samples (Supplementary files – Figures S5 and S6), being the major constituent of these layers.

In order to confirm the visual indications of the SEM micrographs displayed in Figure 4, confocal laser scanning microscopy was employed to measure the surface roughness of the anodized layers. The results are expressed as average roughness (Ra) and mean roughness depth (Rz), as displayed in Table 3. The measurements were made along ten different lines on the sample surface. The anodizing treatment conducted in the borate-containing electrolyte led to the formation of a smoother oxide layer (samples BO-20 and BO-30), as seen in Table 3, confirming the visual aspect shown in Figure 4. The roughness values of the SI-20 and SI-30 samples were the highest, whereas the samples anodized in the phosphate-based electrolyte (PHO-20 and PHO-30) displayed intermediate values. The increase of the applied current density led to an increment of the Ra and Rz values. This effect was less pronounced for the BO-20 and BO-30 samples. Hence, based on the SEM micrographs (Fig 4) and roughness parameters (Table 3), as reported in the literature<sup>38</sup>, the anodized layers were more homogeneous and compact for the borate-containing electrolyte.

Complementary information on the morphology and compactness of the anodized layers was obtained from the cross-sectional SEM micrographs displayed in Figure 5.

**Table 3.** Roughness parameters of the as-received and anodized samples.

Sample	Ra (μm)	Rz (μm)
Uncoated	0.16 ± 0.01	1.52 ± 0.19
SI-20	1.02 ± 0.03	6.56 ± 0.51
SI-30	1.79 ± 0.03	10.2 ± 0.61
PHO-20	0.72 ± 0.09	5.36 ± 0.62
PHO-30	0.92 ± 0.24	6.99 ± 1.40
BO-20	0.37 ± 0.02	3.44 ± 0.36
BO-30	0.40 ± 0.01	3.53 ± 0.63



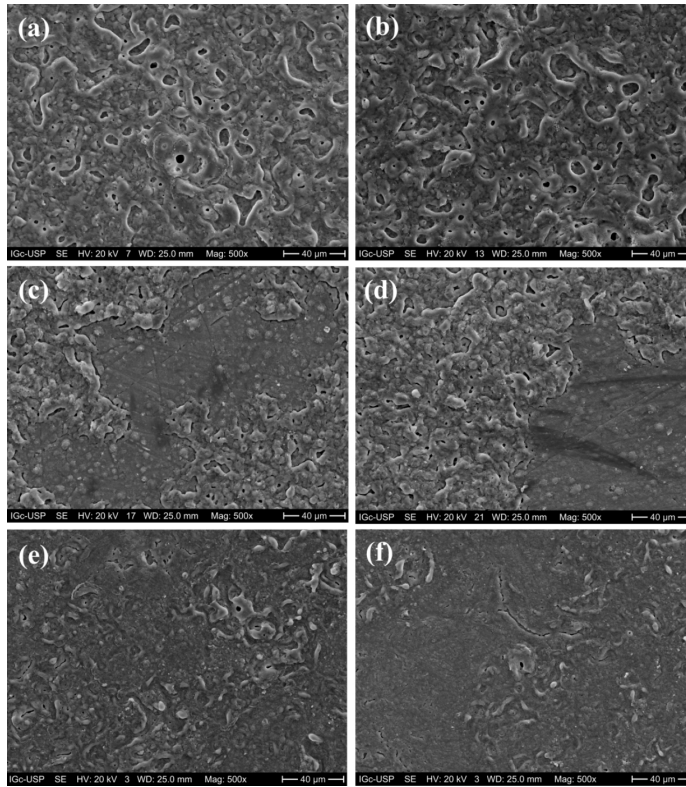


**Figure 4.** SEM micrographs (secondary electrons mode) showing the surface morphologies of the anodized layers: a) SI-20; b) SI-30; c) PHO-20; d) PHO-30; e) BO-20; e) BO-30.

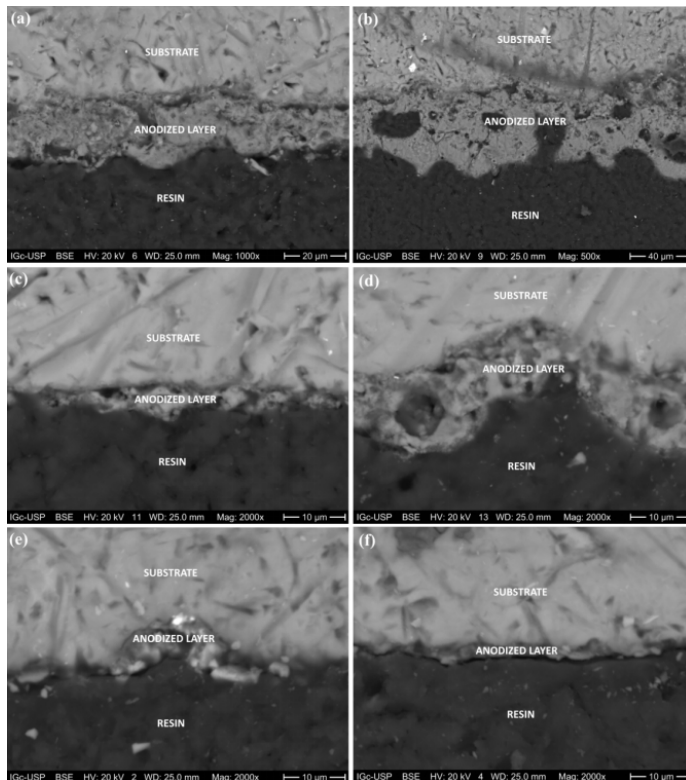


**Figure 5.** SEM micrographs (backscattered electrons mode) showing the cross-section morphologies of the anodized layers: a) SI-20; b) SI-30; c) PHO-20; d) PHO-30; e) BO-20; f) BO-30.

The thickness of the anodized film increased with the applied current density, as observed for the SI-20 (Figure 5a) and SI-30 samples (Figure 5b). Another noticeable feature is that the compactness of the anodic film was also affected by the current density. Figure 5b clearly exhibits discontinuities and an irregular growth of the anodized layer, when compared to Figure 5a. Similar observations are also valid for the PHO-20 (Figure 5c) and PHO-30 (Figure 5d) samples. By increasing the applied current density, the anodic film has grown faster, but showing more defective sites.

A different situation took place when the anodizing treatment was conducted in the borate-containing electrolyte. As observed in Figure 5e and 5f, by increasing the applied current density, the BO-30 sample (Figure 5f) displayed an anodic film more homogeneous and compact with respect to the film obtained for the BO-20 sample (Figure 5e). Furthermore, as mentioned in section 3.1.1, borate ions are associated with a decrease of the electrical conductivity of the anodizing electrolyte, thus leading to the formation of a thinner anodic film, as confirmed by the SEM micrographs displayed in Figure 5e and 5f.

### 3.1.3. XPS analysis

The surface chemical states of the main constituents of the anodized layers were examined by XPS analysis. Figure 6 shows representative Mg 1s high resolution spectra for the SI-20, PHO-20 and BO-20 samples. The spectra for the SI-30, PHO-30 and BO-30 samples present similar features, and are displayed as Supplementary files (Figure S7). The spectra were deconvoluted with three different components. In the case of the SI-30 (Figure 6a) and BO-20 (Figure 6c) the peaks were assigned to  $\text{Mg}(\text{OH})_2$ ,  $\text{MgO}$  and  $\text{Mg}_2\text{SiO}_4$ , in good agreement with other reports<sup>35,46</sup>. The same compounds were observed in the Mg 1s spectra of the SI-30 (Supplementary File - Figure S7a) and BO-30 (Supplementary File - Figure S7c), confirming that  $\text{MgO}$  and  $\text{Mg}_2\text{SiO}_4$  are part of the anodized layers, as also indicated by the XRD patterns displayed in Figure 3. The Mg 1s spectrum of the PHO-20 sample, in turn, presents  $\text{Mg}(\text{OH})_2$ ,  $\text{MgO}$  and  $\text{Mg}_3(\text{PO}_4)_2$ , as seen in Figure 6b. As the anodizing treatment was conducted in a sodium phosphate-based electrolyte, the formation of magnesium phosphate is expected. The peaks are in good agreement with other reports in the literature<sup>47,48</sup>. The same components were also found on the surface of the PHO-30 sample (Supplementary files - Figure S7b). The absence of  $\text{Mg}(\text{OH})_2$  peaks in the XRD patterns of all samples (Figure 3) is likely due to the amorphous nature of this phase.

The Si 2p high resolution spectra were acquired for the samples anodized in silicate-containing electrolytes (SI-20, SI-30, BO-20 and BO-30). One representative Si 2p spectrum is shown in Figure 7 for the BO-20 sample. The Si 2p spectra of the other samples presented the same features, and are displayed as Supplementary files (Figure S8). The spectra were deconvoluted with two components. The low binding energy component was assigned to silicate bonds such as those found in  $\text{Mg}_2\text{SiO}_4$ . The high binding energy component was assigned to silica-type bonds, as observed by other authors<sup>49</sup>.

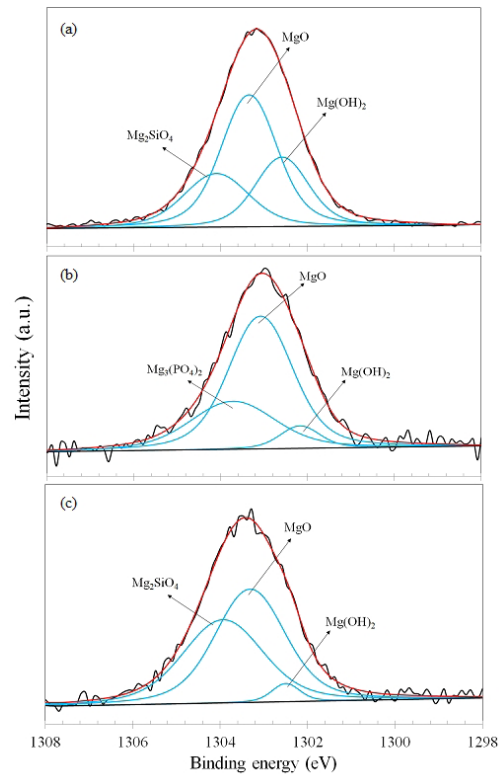


**Figure 6.** XPS Mg 1s high resolution spectra: a) SI-20; b) PHO-20; c) BO-20.

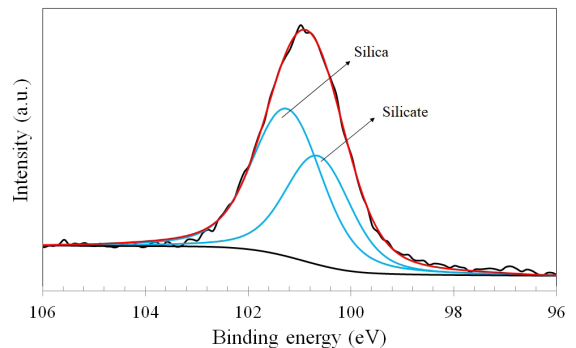


**Figure 7.** XPS Si 2p high resolution spectrum of the BO-20 sample.

A weak B 1s signal was observed in the AZ61 samples anodized in the borate-containing electrolyte. As shown in Figure 8, the B 1s peak appears at approximately 191.6 eV for the BO-20 (Figure 8a) and BO-30 (Figure 8b) samples. This peak is assigned to B-O bonds in the anodized layer, as observed by Ardelean et al.<sup>50</sup>. Oxidation treatments of magnesium alloys in borate-containing electrolytes may lead to the formation of compounds such as  $\text{Mg}_2\text{B}_2\text{O}_5$  or  $\text{Mg}_3\text{B}_2\text{O}_6$ <sup>40,51</sup>. Although not detected by XRD (Figure 3), XPS analysis unequivocally shows that a small amount of borate-containing species is incorporated into the anodic films of BO-20 and BO-30.

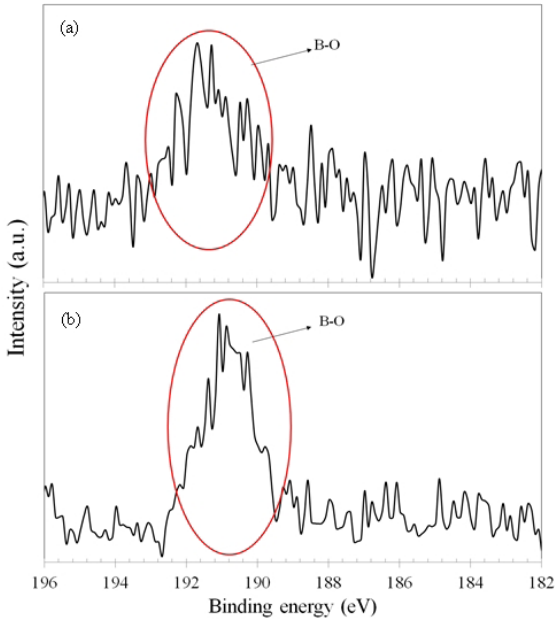


**Figure 8.** XPS B 1s high resolution spectra of the AZ61 alloy anodized in the borate-containing electrolyte: (a) BO-20; b) BO-30.

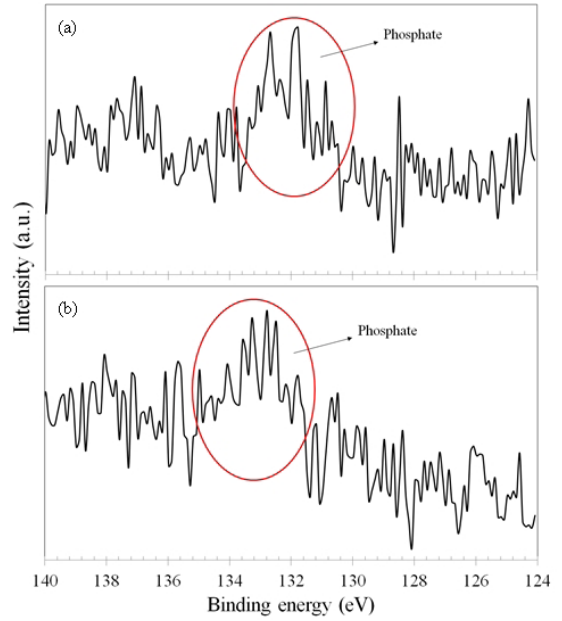


**Figure 9.** XPS P 2p high resolution spectra of the AZ61 alloy anodized in the phosphate-containing electrolyte: (a) PHO-20; b) PHO-30.

The XPS P 2p high resolution spectra of the PHO-20 and PHO-30 samples are shown in Figure 9. For both samples the small peak at approximately 133 eV is assigned to phosphate bonds, in accordance with the literature<sup>52</sup>. The formation of  $\text{Mg}_3(\text{PO}_4)_2$  is expected in this type of process<sup>47,48</sup>. The XPS results confirm the presence of this phase, as also observed in the XRD patterns displayed in Figure 3. The anodized layers on the PHO-20 and PHO-30 samples consist of a mixture of MgO and  $\text{Mg}_3(\text{PO}_4)_2$ , with predominance of MgO, as suggested by the weak XPS signal of the phosphate phase. The presence of amorphous  $\text{Mg}(\text{OH})_2$  cannot be ruled out too.

### 3.2. Corrosion resistance

Potentiodynamic polarization curves of the uncoated and anodized AZ61 alloy are shown in Figure 10. The tests were conducted in 0.1 M NaCl solution at room temperature. Corrosion potential ( $E_{\text{corr}}$ ), corrosion current density ( $i_{\text{corr}}$ ), passive current density ( $i_{\text{pass}}$ ), breakdown potential ( $E_b$ ) and passive range ( $\Delta E = E_b - E_{\text{corr}}$ ) were determined from these curves, as displayed in Table 4. The corrosion current density was determined using the Tafel extrapolation method. Since it is formally valid if both the anodic and cathodic branches are under activation control,  $i_{\text{corr}}$  was determined only for the uncoated AZ61 alloy, as it was the only sample that did not display passivation in the anodic branch of its polarization curve. Conversely, as all anodized samples displayed a passive region,  $i_{\text{pass}}$  was determined instead of  $i_{\text{corr}}$ . It was taken at the middle of the passive range, as proposed by other authors<sup>53</sup>.

As seen in Table 4, the only anodized sample whose  $E_{\text{corr}}$  was shifted to more positive values with respect to the uncoated AZ61 alloy was BO-30. This result is likely related to the compact morphology of the anodic film formed on these samples (Figure 6f), effectively protecting

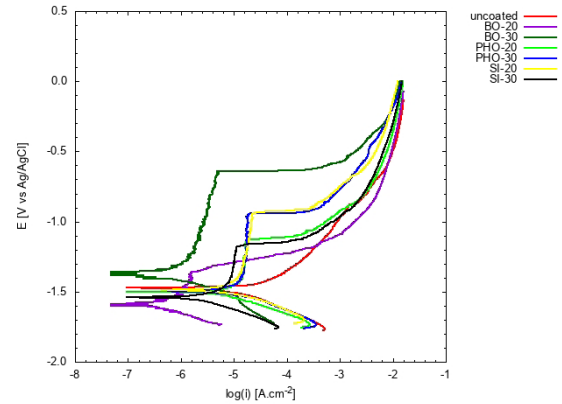


**Figure 10.** Potentiodynamic polarization curves of the uncoated and anodized AZ61 alloy in 0.1 M NaCl solution at room temperature.

the substrate against electrolyte penetration. For the other samples, defects in the coating layers would not provide effective barrier against penetration of corrosive species, thus leading to  $E_{\text{corr}}$  values that are compatible or even more negative than that of the uncoated alloy. In spite of the defective nature of the anodic films formed on some samples, the anodizing treatment promoted a remarkable decrease of the anodic current densities of the AZ61 alloy with respect to the uncoated surface, slowing down its dissolution rate in the 0.1 M NaCl solution. As seen in Figure 10, the electrochemical behavior of the anodized samples was typically passive while that of the bare AZ61 alloy was active. There is a noticeable trend of decreasing the values of  $i_{\text{pass}}$  for the samples anodized in the borate-containing electrolyte (BO-20 and BO-30), as displayed in Table 4.

**Table 4.** Electrochemical parameters of the uncoated and anodized AZ61 alloy obtained from the potentiodynamic polarization curves shown in Figure 11.

Sample	$E_{\text{corr}}$ (mV <sub>Ag/AgCl</sub> )	$E_b$ (mV <sub>Ag/AgCl</sub> )	$\Delta E$ (mV)	$i_{\text{corr}}$ ( $\mu\text{A}\cdot\text{cm}^{-2}$ )	$i_{\text{pass}}$ ( $\mu\text{A}\cdot\text{cm}^{-2}$ )
Uncoated	$-1473 \pm 43$	----	----	$6.0 \pm 0.7$	-
SI-20	$-1487 \pm 66$	$-929 \pm 26$	$558 \pm 42$	----	$17.8 \pm 3.1$
SI-30	$-1540 \pm 82$	$-1192 \pm 45$	$348 \pm 29$	----	$7.9 \pm 1.4$
PHO-20	$-1502 \pm 58$	$-1148 \pm 87$	$354 \pm 34$	----	$15.8 \pm 2.0$
PHO-30	$-1497 \pm 42$	$-951 \pm 128$	$546 \pm 57$	----	$17.8 \pm 1.7$
BO-20	$-1601 \pm 86$	$-1398 \pm 62$	$203 \pm 16$	----	$1.0 \pm 0.3$
BO-30	$-1383 \pm 44$	$-652 \pm 38$	$731 \pm 37$	----	$3.2 \pm 0.5$

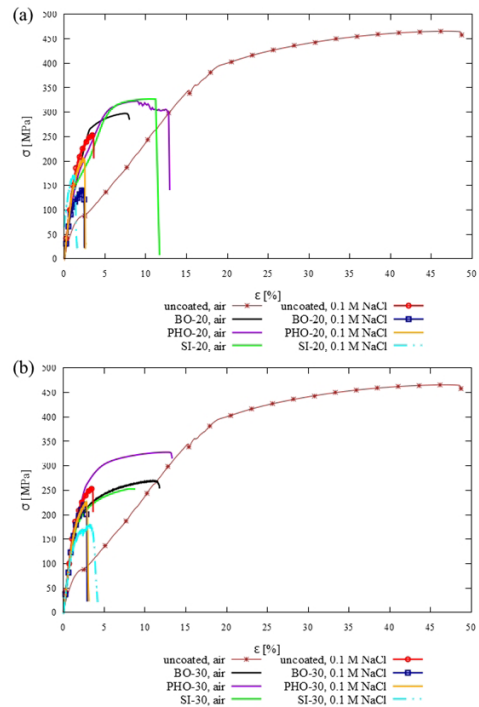
**Table 5.** Tensile properties and susceptibility indices of the uncoated and anodized AZ61 alloy for tests conducted in air and 0.1 M NaCl solution at room temperature.

Sample	Ultimate tensile strength (UTS)			Elongation at break ( $\epsilon$ )		
	Air (MPa)	0.1 M NaCl (MPa)	$I_{\text{SCC}}$	Air (%)	0.1 M NaCl (%)	$I_{\epsilon}$
Uncoated	$466 \pm 5$	$254 \pm 12$	$0.45 \pm 0.02$	$46.7 \pm 2.3$	$3.4 \pm 0.2$	$0.93 \pm 0.01$
SI-20	$327 \pm 7$	$169 \pm 8$	$0.48 \pm 0.01$	$10.4 \pm 1.2$	$1.2 \pm 0.5$	$0.89 \pm 0.01$
SI-30	$253 \pm 10$	$177 \pm 10$	$0.30 \pm 0.01$	$8.0 \pm 0.4$	$3.2 \pm 0.3$	$0.60 \pm 0.01$
PHO-20	$323 \pm 11$	$204 \pm 7$	$0.36 \pm 0.01$	$8.8 \pm 0.5$	$2.4 \pm 0.1$	$0.73 \pm 0.01$
PHO-30	$328 \pm 9$	$225 \pm 14$	$0.31 \pm 0.02$	$12.5 \pm 0.6$	$2.8 \pm 0.1$	$0.78 \pm 0.01$
BO-20	$297 \pm 14$	$142 \pm 6$	$0.52 \pm 0.01$	$7.5 \pm 0.4$	$2.3 \pm 0.3$	$0.70 \pm 0.01$
BO-30	$269 \pm 3$	$223 \pm 2$	$0.17 \pm 0.01$	$11.0 \pm 1.2$	$2.7 \pm 0.4$	$0.75 \pm 0.01$

This result can be related with the smooth and compact morphology of the anodic films formed on these samples, as shown in section 3.1.2. Moreover, it is evident that BO-30 presents the largest values of passive range ( $\Delta E$ ) and breakdown potential ( $E_b$ ), indicating its anodic film is the most corrosion resistant. In fact, this result confirms what was expected from the SEM micrographs displayed in section 3.1.2, revealing that the borate-containing electrolyte promoted the formation of a thin, compact and corrosion resistant anodized layer. The corrosion resistance of the samples anodized in the silicate (SI-20 and SI-30) and phosphate (PHO-20 and PHO-30) electrolytes was lower, as indicated by the larger values of  $i_{\text{pass}}$  in comparison with those of the BO-20 and BO-30 samples (Table 4). The cracks and pores of the anodic films on these samples (Figure 4a-d and Figure 5a-d) can explain their lower corrosion protection ability.

### 3.3. Tensile tests in air and 0.1 M NaCl solution

Figure 11 displays the engineering stress versus engineering strain curves of the uncoated and anodized AZ61 alloy for tensile tests conducted in air and 0.1 M NaCl solution. Tensile properties such as the ultimate tensile strength (UTS) and elongation at break were determined from these curves, and are presented in Table 5. Furthermore, the susceptibility indices  $I_{\text{SCC}}$  and  $I_{\epsilon}$  were calculated according to equations (1) and (2), and are also displayed in this table.

**Figure 11.** Engineering stress versus engineering strain curves of the uncoated and anodized AZ61 alloy in air and 0.1 M NaCl solution: a) anodization at 20 mA.cm<sup>-2</sup>; b) anodization at 30 mA.cm<sup>-2</sup>.



Two general aspects are evident from Figure 11. Firstly, for the tests conducted in air, anodization significantly reduced the UTS and ductility of the AZ61 alloy, independently of the composition of the anodizing electrolyte. Secondly, when the tests were conducted in 0.1 M NaCl solution, the corrosive environment reduced the UTS and ductility of the alloy, either uncoated or anodized. In fact, the reduction of ductility was up to nine times after anodization for the tests conducted in air. In 0.1 M solution, in turn, this effect was less marked, as the ductility of the anodized samples was not significantly reduced with respect to the uncoated AZ61 alloy. This behavior suggests that the anodized layer acts as a stress riser, triggering the propagation of tensile cracks, and leading to fracture with a reduced level of plastic deformation, as reported by other authors<sup>24</sup>.

The effect of the anodizing current density on the SCC behavior of the AZ61 alloy can be inferred from the susceptibility indices displayed in Table 5. From the values of  $I_e$  (susceptibility index for the elongation at break), it is clear that the increase of the current density did not present a significant effect on this index for the samples anodized in the borate and phosphate-based electrolytes. As mentioned before, the susceptibility to SCC increases as the index approaches unity. The most noticeable change of  $I_e$  with the increase of current density was observed for SI-20 and SI-30. As shown in Table 5,  $I_e$  decreased for SI-30 with respect to SI-20, implying that the susceptibility to SCC decreased when anodization was conducted at 30 mA.cm<sup>-2</sup> for the samples treated in 3 M KOH + 0.15 M Na<sub>2</sub>SiO<sub>3</sub> solution.

From the cross-sectional SEM micrographs shown in Figure 5a and 5b, one could expect the defective and irregular morphology of the anodized layer formed on the SI-30 would facilitate electrolyte penetration. This, in turn, could increase the susceptibility of the AZ61 alloy to SCC by intensifying pitting formation at the interface substrate/anodic film. However, such effect was not observed. A possible explanation may be related to the fact that SI-30 sample displayed the lowest values of UTS, and a low elongation at break (the second lowest among all anodized samples). Hence, as the defective anodized layer had already greatly decreased its tensile properties in air, the presence of the corrosive environment did not lead to a significant deterioration of these properties with respect to SI-20. This effect also manifests if one looks at the values of  $I_{SCC}$  (susceptibility index for the UTS). The value of  $I_{SCC}$  decreased for SI-30 with respect to SI-20. For the samples anodized in the phosphate-based electrolyte (PHO-20 and PHO-30) the  $I_{SCC}$  was not significantly altered when the anodizing current density increased. The major influence of the current density on  $I_{SCC}$  was observed for the samples anodized in the borate-containing electrolyte. As shown in Table 5, the  $I_{SCC}$  of BO-30 reduced almost three times with respect to BO-20. Such lower susceptibility to SCC may be related to the compactness of the anodic film formed on this sample (section 3.1.2). Pores and cracks of the anodic layer, as well as the intrinsic brittleness of this ceramic layer, are associated with its limited ability to enhance the SCC behavior of anodized metallic substrates<sup>54</sup>.

The oxide layers could effectively slow down the corrosion kinetics of the AZ61 alloy, depending on the anodizing conditions, as shown in Figure 10 by the remarkable reduction of the anodic currents with respect to the uncoated substrate. Conversely, the mechanical strength was reduced after anodizing, as denoted by the values of UTS and elongation at break in the tensile tests conducted in air. Thus, the anodic films play two distinct roles, if one considers the electrochemical and mechanical effects separately. The decrease of the anodic currents indicates that the oxide films act as a barrier against electrolyte penetration, even though they are intrinsically permeated by pores and cracks (Figure 4 and 5). Simultaneously, it is accompanied by the stress riser effect that decreased both the tensile strength and ductility. Additionally, the susceptibility to SCC ( $I_{SCC}$  values shown in Table 5) can be correlated with the electrochemical behavior described in section 3.2. As discussed above, the  $I_{SCC}$  values were affected by the morphological aspects of the anodic films, being reduced for the most compact anodized layers (BO-30). In the same regard, the passive range and breakdown potentials were also dependent on the compactness of the anodized layer, being maximized for the BO-30 sample. Hence, there is an evident correlation between the SCC susceptibility and the electrochemical stability of the oxide film, and the compactness of the anodizing layer play a central role in this scenario.

### 3.4. Fracture surfaces

SEM micrographs of the fracture surfaces of the uncoated AZ61 alloy after the tensile tests in air and 0.1 M NaCl solution are shown in Figure 12. For the test conducted in air (Figure 12a) there is a long crack propagation region, typically associated with ductile behavior, as also indicated in the stress-strain curve of this sample (Figure 11). The SEM micrograph shown in Figure 12c confirms the ductile character of the fracture surface by the unequivocal presence of dimples on the crack propagation region, as also reported by Srinivasan et al.<sup>55</sup> for the AZ61 alloy. The side view of the fractured specimen (Figure 12e) shows a slant fracture with a slope of approximately 45°, typical of ductile specimens subjected to tensile tests<sup>56</sup>. Some distinct aspects may be seen in the case of the specimen fractured in the 0.1 M NaCl solution. The general aspect of the fracture surface (Figure 12b) displays smoother sites when compared to the specimen fractured in the air (Figure 12a), suggesting a mixed ductile-brittle fracture mode. In fact, the microfractographic features of this sample (Figure 12d) indicate the coexistence of ductile (dimpled fracture) and brittle (cleavage regions at the right side of the micrograph) features, characterizing the mixed fracture mode. By comparing the side view (Figure 12f) with that of the specimen fractured in the air (Figure 12e), the reduction of the ductile character of the fracture surface is also evident, as indicated by the relatively flat fracture. Hence, Figure 12 shows the susceptibility of the AZ61 alloy to SCC, as also inferred from the values of  $I_{SCC}$  and  $I_e$  (Table 5) for the uncoated substrate, corroborating literature reports<sup>57</sup>.

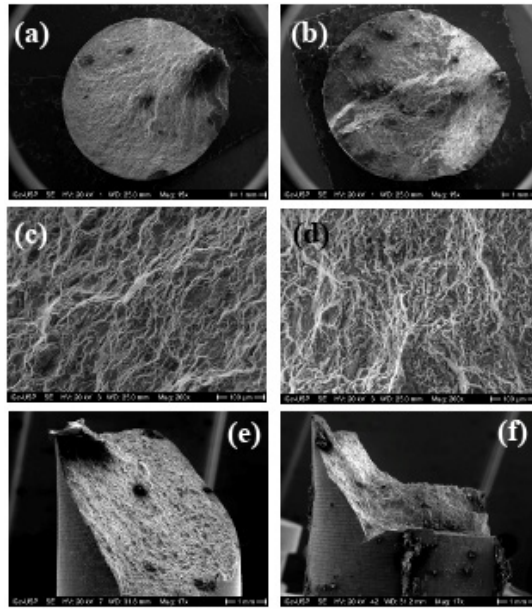


**Figure 12.** SE-SEM micrographs of the fracture surfaces of the as-received AZ61 alloy: a) cross-section; specimen tested in air; b) cross section; specimen tested in 0.1 M NaCl solution; c) high magnification view of (a); d) high magnification view of (b); e) side view; specimen tested in air; f) side view; specimen tested in 0.1 M NaCl.

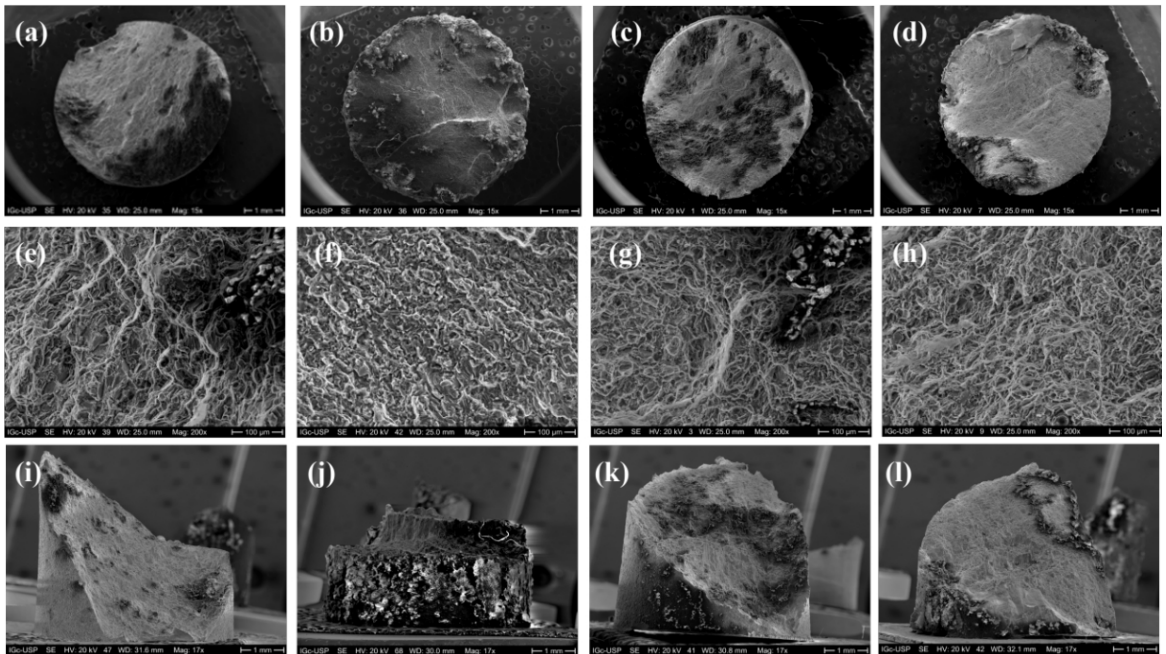


**Figure 13.** SE-SEM micrographs of the fracture surfaces of the SI-20 and SI-30 samples: a) SI-20 cross-section; specimen tested in air; b) SI-20 cross section; specimen tested in 0.1 M NaCl solution; c) SI-30 cross-section; specimen tested in air; d) SI-30 cross section; specimen tested in 0.1 M NaCl solution; e) high magnification view of (a); f) high magnification view of (b); g) high magnification view of (c); h) high magnification view of (d); i) SI-20 side view; specimen tested in air; j) SI-20 side view; specimen tested in 0.1 M NaCl; k) SI-30 side view; specimen tested in air; l) SI-30 side view; specimen tested in 0.1 M NaCl.

The fracture surfaces of the SI-20 and SI-30 samples are shown in Figure 13. The general aspect of the fracture surface of the SI-20 sample tested in the air (Figure 13a) displays a wide crack propagation region, indicating the ductile character of this sample, as also confirmed by the

dimpled fracture observed in Figure 13e. Its side view (Figure 13i) also displays the slant fracture typical of ductile behavior. When this sample was fractured in 0.1 M NaCl solution the fracture surface exhibits different aspects. As seen in Figure 13b (general fracture surface) and 13f

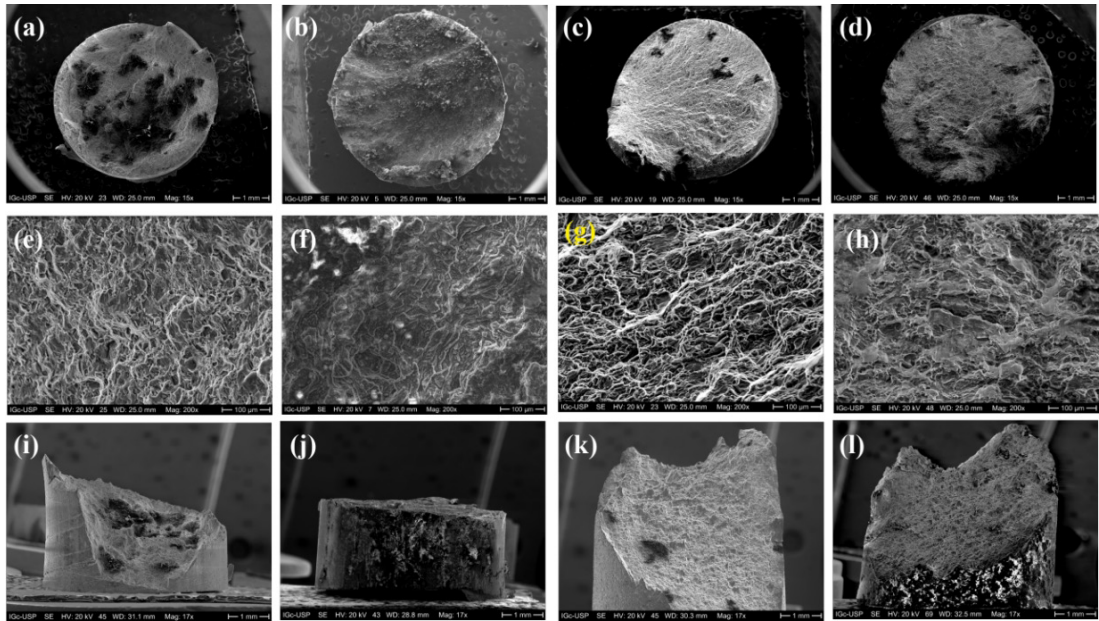


**Figure 14.** SE-SEM micrographs of the fracture surfaces of the PHO-20 and PHO-30 samples: a) PHO-20 cross-section; specimen tested in air; b) PHO-20 cross section; specimen tested in 0.1 M NaCl solution; c) PHO-30 cross-section; specimen tested in air; d) PHO-30 cross section; specimen tested in 0.1 M NaCl solution; e) high magnification view of (a); f) high magnification view of (b); g) high magnification view of (c); h) high magnification view of (d); i) PHO-20 side view; specimen tested in air; j) PHO-20 side view; specimen tested in 0.1 M NaCl; k) PHO-30 side view; specimen tested in air; l) PHO-30 side view; specimen tested in 0.1 M NaCl.

(microfractographic features), smooth regions and a granular aspect, typical of brittle fractures were observed for the SI-20 sample in 0.1 M NaCl solution. The side view displayed in Figure 13j clearly indicates an intense deterioration of the fractured specimen and the flat fracture associated with brittle failure, differently from what was observed for the specimen fractured in the air (Figure 13i).

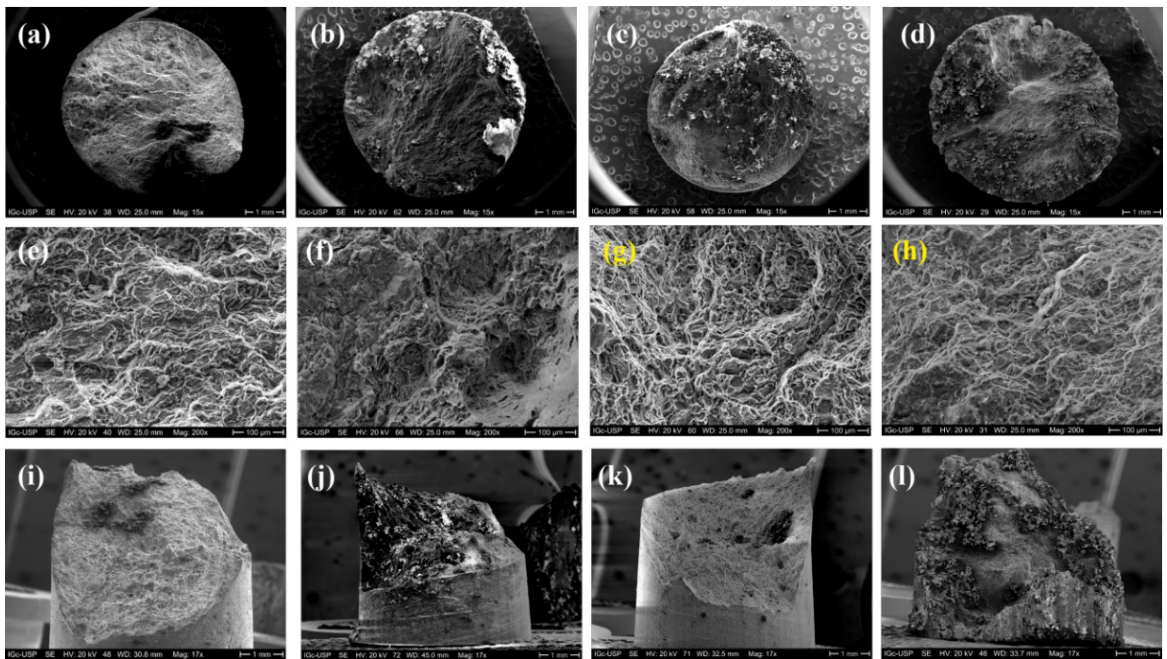
Similar features could be found in the fracture surfaces of the SI-30 sample. The general view (Figure 13c) and microfractographic features (Figure 13g) typically show a wide crack propagation region and a dimpled fracture, respectively. The side view (Figure 13k) also shows a slant fracture associated with a ductile fracture mode. When the tests were conducted in 0.1 M NaCl solution, some localized cleavage sites could be seen, as displayed in the left side of Figure 13h. The side view of the SI-30 sample tested in the NaCl solution (Figure 13l) still shows a predominant slant fracture, suggesting the increase of the anodizing current density did not alter the fracture mode with respect to the SI-20 condition. This result is in agreement with the  $I_{SCC}$  and  $I_g$  values of the SI-20 and SI-30 samples (Table 5), that indicated a reduction of the susceptibility to SCC of SI-30 with respect to SI-20.

The corrosive environment had a remarkable effect on the mechanical behavior of the samples anodized in the 3 M KOH + 0.5 M  $\text{Na}_3\text{PO}_4$  solution (PHO-20 and PHO-30). This can be inferred from the SEM micrographs shown in Figure 14.

By examining the fracture surface of the PHO-20 sample in the air (Figure 14e) and in 0.1 M NaCl solution (Figure 14f), the microfractographic features changed from dimpled to cleavage fracture, indicating the susceptibility of this sample to SCC.

The general aspects of the fracture surface (Figure 14a and 14b) point to this direction too, as seen by the presence of granular regions on the specimen fractured in the sodium chloride solution (Figure 14b). Furthermore, ductility loss of the PHO-20 sample in the corrosive environment is also evident from the side views displayed in Figure 14i and 14j. Fracture exhibited a flat character for the test conducted in the sodium chloride solution (Figure 14j). Sample PHO-30 also exhibits a trend of increasing the cleavage character of the fracture surface when the test was conducted in the sodium chloride solution. Nonetheless, some distinct aspects can be highlighted with respect to PHO-20. The most striking difference seems to be associated with the ductility level, either for the test conducted in the air or in the 0.1 M NaCl electrolyte. The dimples formed on the fracture surface of the PHO-30 sample tested in air (Figure 14g) are more pronounced than those on the surface of the PHO-20 sample in the same environment (Figure 14c). Similarly, for the tests conducted in the corrosive environment, PHO-30 still shows some dimples on the fracture surface (Figure 14h), while it was mainly flat for the PHO-20 sample (Figure 14f), losing the dimpled fracture mode. Thus, as the anodizing current density increased, the susceptibility to SCC decreased for the samples treated in the phosphate electrolyte. This is also confirmed by the slant fracture of the PHO-30 sample either in the air or in the sodium chloride solution (Figure 14k and 14l, respectively) with respect to the predominantly flat fracture of the PHO-20 sample in both conditions (Figure 14i and 14j). The increase of the localized corrosion protection ability of PHO-30 when compared to PHO-20, as indicated by its larger values of breakdown potential and passive range (Table 4), may be related to its enhanced SCC behavior.





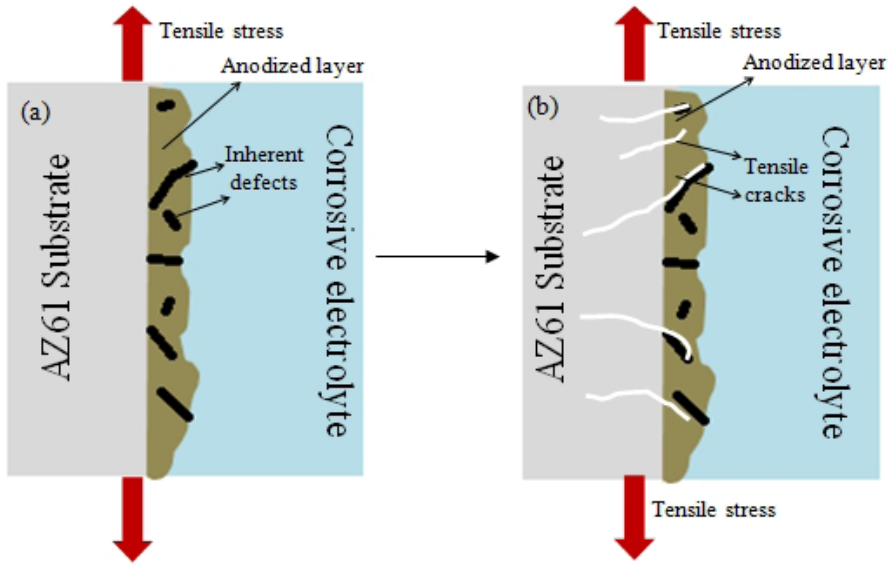
**Figure 15.** SE-SEM micrographs of the fracture surfaces of the BO-20 and BO-30 samples: a) BO-20 cross-section; specimen tested in air; b) BO-20 cross section; specimen tested in 0.1 M NaCl solution; c) BO-30 cross-section; specimen tested in air; d) BO-30 cross section; specimen tested in 0.1 M NaCl solution; e) high magnification view of (a); f) high magnification view of (b); g) high magnification view of (c); h) high magnification view of (d); i) BO-20 side view; specimen tested in air; j) BO-20 side view; specimen tested in 0.1 M NaCl; k) BO-30 side view; specimen tested in air; j) BO-30 side view; specimen tested in 0.1 M NaCl.

Figure 15 shows the fracture surfaces of the BO-20 and BO-30 samples for the tests conducted in the air and 0.1 M NaCl solution. The general aspect of the fracture surface of the BO-20 sample tested in air (Figure 15a) and the microfractographic features (Figure 15e) reveal a mixed fracture mode, with the concomitant presence of dimples and cleavage sites. The same features can be observed for the BO-30 sample tested in air (Figure 15c and 15g), although the dimples occupy a bigger area. The side views displayed in Figure 15i and 15k show the slant fracture typical of ductile behavior. The corrosive environment had a remarkable effect on the fractographic aspects of the BO-20 sample, as well as for the samples anodized in the phosphate-based electrolyte, as suggested by the micrographs displayed in Figure 15b and 15f. The fracture surface has several craters originated from alloy dissolution upon exposure to the sodium chloride solution. The side view displayed in Figure 15j suggests a strong degradation when the BO-20 sample was tested in the sodium chloride solution. By examining the fracture surface of the BO-30 sample, its general aspect (Figure 15d) and microfractographic features (Figure 15h) reveal loss of ductility in comparison with the sample tested in air (Figure 15c and 15g). The dimpled aspect of the fracture surface is less pronounced for the sample tested in the sodium chloride solution. The presence of smooth regions, typical of brittle fracture (cleavage mode), is observed, although some dimples can still be seen (Figure 15g). The side view shown in Figure 15l also indicates intense deterioration, as well as observed for the BO-20 sample (Figure 15j). Such behavior reflects what was inferred from the results displayed in Table 5 that

indicated larger susceptibility of the BO-20 sample to SCC ( $I_{SCC}$  and  $I_e$  values) with respect to BO-30. Furthermore, the ductility loss of the AZ61 alloy, as observed from the stress-strain curves in Figure 11, is also reflected on the fractographic features, with a predominance of cleavage areas over dimpled fracture. Hence, by increasing the anodizing current density in the borate-containing electrolyte, the AZ61 alloy became less prone to SCC. This behavior can be explained by the SEM micrographs shown in section 3.1.2, which revealed the formation of a thin, compact and homogeneously distributed anodic film for the BO-30 sample. This morphology favored both the corrosion resistance (Figure 10) and SCC behavior of the AZ61 substrate.

Based on the fractographic analysis and SSRT results (section 3.3), the SCC behavior of the anodized AZ61 alloy is schematically illustrated in Figure 16. The anodized film exhibits intrinsic defects (pores and cracks) that may act as diffusive pathways for corrosive species from the electrolyte to reach the metallic substrate (Figure 16a). Furthermore, when the tensile stress is applied during the slow strain rate tests, these defects act as stress risers, decreasing the mechanical strength and ductility of the AZ61 alloy. Crack propagation preferentially occurs along these sites, leading to the final failure (Figure 16b). Brittle fracture is the dominant failure mode in the presence of the corrosive electrolyte. The compactness of the oxide layer affected the susceptibility to SCC. A thin, compact anodized layer, such as that formed on the BO-30 sample, is able to greatly reduce the anodic dissolution rate of the AZ61 alloy and, concomitantly, make it less prone to SCC.





**Figure 16.** Schematic illustration of the SCC behavior of the anodized AZ61 in 0.1 M NaCl solution: a) Anodized AZ61 alloy immersed in the corrosive electrolyte and subjected to tensile stress. The anodized layer is permeated by inherent defects formed during the electrolytic oxidation process; b) Inherent defects of the anodized layer act as stress risers, being the preferential sites for crack nucleation and growth.

#### 4. Conclusions

In this work, the effect of anodization on the stress corrosion cracking behavior of the AZ61 magnesium alloy was assessed in 0.1 M NaCl solution. The main conclusions can be drawn as follows:

- i) In the case of the anodic films obtained in the 3 M KOH + 0.50 M Na<sub>2</sub>SiO<sub>3</sub>, the anodized layers consisted of a mixture of MgO, Mg<sub>2</sub>SiO<sub>4</sub> and Mg(OH)<sub>2</sub>. The same compounds were also observed for the samples anodized 3 M KOH + 0.15 M Na<sub>2</sub>SiO<sub>3</sub> + 0.1 M Na<sub>2</sub>B<sub>4</sub>O<sub>7</sub>·10H<sub>2</sub>O solution, for which B-O bonds were also detected, as shown by XPS analysis. The anodic films formed on the 3 M KOH + 0.5 M Na<sub>3</sub>PO<sub>4</sub> solution consisted of a mixture of MgO, Mg<sub>3</sub>(PO<sub>4</sub>)<sub>2</sub> and Mg(OH)<sub>2</sub>.
- ii) The anodic films formed on the borate-containing electrolyte were thinner, more compact and homogeneous than those obtained in the other electrolytes.
- iii) The increment of the anodizing current density promoted an increase of the anodic film thickness.
- iv) The corrosion resistance was favored for the samples anodized in the borate-containing electrolyte due to the more compact morphology of the anodic films.
- v) The presence of the anodic films greatly decreased the ultimate tensile strength and ductility of the AZ61.
- vi) The susceptibility to SCC was dependent on the morphology of the anodic films. The lowest susceptibility indices ( $I_{SCC}$  and  $I_e$ ) were obtained for the sample anodized in the borate-containing electrolyte at 30 mA.cm<sup>-2</sup>. It was also the sample with the best corrosion resistance, according to the potentiodynamic polarization curves.

#### 5. Acknowledgments

Authors are grateful to CNPq for the financial support to this work (Process 406307/2018-0). Fábio Okamoto is thankful to CAPES for the research grant (Finance Code 001). The Multiuser Experimental Facilities (CEM-UFABC) are acknowledged for the experimental support.

#### 6. References

1. Zhao T, Wang Z, Feng Y, Li Q. Synergistic corrosion inhibition of sodium phosphate and sodium dodecyl sulphate on magnesium alloy AZ91 in 3.5 wt% NaCl solution. *Mater Today Commun.* 2022;31:103568.
2. Zagar S, Soyama H, Grum J, Sturm R. Surface integrity of heat treatable magnesium alloy AZ80A after cavitation peening. *J Mater Res Technol.* 2022;17:2098-107.
3. Osipenko MA, Kharytonau DS, Kasach AA, Ryl R, Adamiec J, Kurilo II. Inhibitive effect of sodium molybdate on corrosion of AZ31 magnesium alloy in chloride solutions. *Electrochim Acta.* 2022;414:140175.
4. Liu H, Cao F, Song G-L, Zheng D, Shi Z, Dargusch MS, et al. Review of the atmospheric corrosion of magnesium alloys. *J Mater Sci Technol.* 2019;35:2003-16.
5. Hu C, Le Q, Zhou X, Cheng C, Guo R, Li X, et al. The growth and corrosion mechanism of Zn-based coating on AZ31 magnesium alloys by novel hot-dip process. *Mater Charact.* 2022;189:111988.
6. Witte F, Hort N, Vogt C, Cohen S, Kainer KU, Willumeit R, et al. Degradable biomaterials based on magnesium corrosion. *Curr Opin Solid State Mater Sci.* 2008;12:63-72.
7. Zhao D, Witte F, Lu F, Wang J, Li J, Qin L. Current status on clinical applications of magnesium-based orthopaedic implants: a review from clinical translational perspective. *Biomaterials.* 2017;112:287-302.
8. Mousavian SMH, Tabaian SH. The effect of anodizing electrolyte composition on electrochemical properties of anodized magnesium. *Anti-Corros Methods Mater.* 2022;69:194-203.

9. Heakal FE-T, Shehata OS, Bakry AM, Tantawy NS. Influence of anodization and bovine serum albumin on the degradation of new AXJ-magnesium alloy system as a bioabsorbable orthopedic implant. *J Electroanal Chem (Lausanne)*. 2022;918:116458.
10. Pan S, Tu X, Yu J, Zhang Y, Miao C, Xu Y, et al. Optimization of AZ31B magnesium alloy anodizing process in NaOH- $\text{Na}_2\text{SiO}_3$ - $\text{Na}_2\text{B}_4\text{O}_7$  environmental-friendly electrolyte. *Coatings*. 2022;12:578.
11. Kim S-J, Okido M, Mizutani Y, Ichino R, Tanikawa S, Hasegawa S. Formation of anodic films on Mg-Al alloys in NaOH solutions at constant potentials. *Mater Trans*. 2003;44:1036-41.
12. Salman SA, Ichino R, Okido M. Improvement of corrosion resistance of AZ31 Mg alloy by anodizing with co-precipitation of cerium oxide. *Trans Nonferrous Met Soc China*. 2009;19:883-6.
13. Li W, Zhu L, Liu H. Effects of silicate concentration on anodic films formed on AZ91D magnesium alloy in solution containing silica sol. *Surf Coat Tech*. 2006;201:2505-11.
14. Oliveira LA, Silva RMP, Rodas ACD, Souto RM, Antunes RA. Surface chemistry, film morphology, local electrochemical behavior and cytotoxic response of anodized AZ31B magnesium alloy. *J Mater Res Technol*. 2020;9:14754-70.
15. Fukuda H, Matsumoto Y. Effects of  $\text{Na}_2\text{SiO}_3$  on anodization of Mg-Al-Zn alloy in 3 M KOH solution. *Corros Sci*. 2004;46:2135-42.
16. Hsiao H-H, Chung P, Tsai W-T. Baking treatment effect on materials characteristics and electrochemical behavior of anodic film formed on AZ91D magnesium alloy. *Corros Sci*. 2007;49:781-93.
17. Liu Y, Wei Z, Yang F, Zhang Z. Environmental friendly anodizing of AZ91D magnesium alloy in alkaline borate-benzoate electrolyte. *J Alloys Compd*. 2011;509:6440-6.
18. Al Bacha S, Aubert I, Zakhour M, Nakhl M, Bobet J-L. Hydrolysis properties, corrosion behavior and microhardness of AZ91 "model" alloys. *J Alloys Compd*. 2020;845:156283.
19. Acharya MG, Shetty AN. The corrosion behavior of AZ31 alloy in chloride and sulfate media: a comparative study through electrochemical investigations. *Journal of Magnesium and Alloys*. 2019;7:98-112.
20. Jafari S, Raman RKS. In-vitro biodegradation and corrosion-assisted cracking of a coated magnesium alloy in modified-simulated body fluid. *Mater Sci Eng C*. 2017;78:278-87.
21. Padekar BS, Raja VS, Raman RKS, Lyon P. Stress corrosion cracking behavior of magnesium alloys EV31A and AZ91E. *Mater Sci Eng A*. 2013;583:169-76.
22. Winzer N, Atrens A, Dietzel W, Song G, Kainer KU. Fractography of stress corrosion cracking of Mg-Al alloys. *Metall Mater Trans, A Phys Metall Mater Sci*. 2008;39:1157-73.
23. Cao F, Shi Z, Song G-L, Liu M, Dargusch MS, Atrens A. Stress corrosion cracking of several solution heat-treated Mg-X alloys. *Corros Sci*. 2015;96:121-32.
24. Srinivasan PB, Blawert C, Dietzel W. Effect of plasma electrolytic oxidation treatment on the corrosion and stress corrosion cracking behavior of AM50 magnesium alloy. *Mater Sci Eng A*. 2008;494:401-6.
25. Khan SA, Miyashita Y, Mutoh Y. Corrosion fatigue behavior of AM60 magnesium alloy with anodizing layer and chemical-conversion-coating layer. *Mater Corros*. 2015;66:940-8.
26. Srinivasan PB, Blawert C, Dietzel W, Kainer KU. Stress corrosion cracking behaviour of a surface-modified magnesium alloy. *Ser Mater*. 2008;59:43-6.
27. Srinivasan PB, Blawert C, Dietzel W. Effect of plasma electrolytic oxidation coating on the stress corrosion cracking behaviour of wrought AZ61 magnesium alloy. *Corros Sci*. 2008;50:2415-8.
28. ASTM: American Society for Testing and Materials. ASTM B107/B107M-13: standard specification for magnesium-alloy extruded bars, rods, profiles, tubes, and wire. West Conshohocken: ASTM; 2013.
29. ASTM: American Society for Testing and Materials ASTM B557-15: standard test methods for tensile testing wrought and cast aluminum- and magnesium-alloy product (metric). West Conshohocken: ASTM; 2015.
30. ASTM: American Society for Testing and Materials ASTM E8/E8M-16a: standard test methods for tensile testing of metallic materials. West Conshohocken: ASTM; 2016.
31. ASTM: American Society for Testing and Materials ASTM G1-90: standard practice for preparing, cleaning, and evaluation corrosion test specimens. West Conshohocken: ASTM; 2003. p. 1-9.
32. Peron M, Bertolini R, Cogo S. On the corrosion, stress corrosion and cytocompatibility performances of ALD  $\text{TiO}_2$  and  $\text{ZrO}_2$  coated magnesium alloys. *J Mech Behav Biomed Mater*. 2022;125:104945.
33. Choudhary L, Raman RKS, Hofstetter J, Uggowitzer PJ. In-vitro characterization of stress corrosion cracking of aluminium-free magnesium alloys for temporary bio-implant applications. *Mater Sci Eng C*. 2014;42:629-36.
34. Bai A, Chen Z-J. Effect of electrolyte additives on anti-corrosion ability of micro-arc oxide coatings formed on magnesium alloy AZ91D. *Surf Coat Tech*. 2009;203:1956-63.
35. Gao H, Zhang M, Yang X, Huang P, Xu K. Effect of  $\text{Na}_2\text{SiO}_3$  solution concentration of micro-arc oxidation process on lap-shear strength of adhesive-bonded magnesium. *Appl Surf Sci*. 2014;314:447-52.
36. Ahn BH, Song JI, Koo BH. Effect of electrolyte on mechanical properties of AZ31B Mg alloy in electrolytic plasma processing. *Trans Nonferrous Met Soc China*. 2014;24:s125-8.
37. Duan H, Yan C, Wang F. Effect of electrolyte additives on performance of plasma electrolytic oxidation films formed on magnesium alloy AZ91D. *Electrochim Acta*. 2007;52:3785-93.
38. Wu H-I, Cheng Y-L, Li L-L, Chen Z-H, Wang H-M, Zhang Z. The anodization of ZK60 magnesium alloy in alkaline solution containing silicate and the corrosion properties of the anodized films. *Appl Surf Sci*. 2007;253:9387-94.
39. Si Y, Xiong Z, Zheng X, Li M, Yang Q. Improving the anti-corrosion ability of anodization film of AZ31B magnesium alloy by addition of  $\text{NH}_4\text{VO}_3$  in the electrolyte. *Int J Electrochem Sci*. 2016;11:3261-8.
40. Zhang RF, Zhang SF, Shen YL, Zhang LH, Liu TZ, Zhang YQ, et al. Influence of sodium borate concentration on properties of anodic coatings obtained by micro arc oxidation on magnesium alloys. *Appl Surf Sci*. 2012;258:6602-10.
41. Durdu S, Aytaç A, Usta M. Characterization and corrosion behavior of ceramic coating on magnesium by micro-arc oxidation. *J Alloys Compd*. 2011;509:8601-6.
42. Anawati A, Hidayati E, Labibah H. Characteristics of magnesium phosphate coatings formed on AZ31 Mg alloy by plasma electrolytic oxidation with improved current efficiency. *Mater Sci Eng B*. 2021;272:115354.
43. El Mahallawy NA, Shoeib MA, Abouelenain MH. AZ91 magnesium alloys: anodizing of using environmental friendly electrolytes. *J Surf Eng Mater Adv Technol*. 2011;1:62-72.
44. Oliveira LA, Silva RMP, Rodas ACD, Souto RM, Antunes RA. Surface chemistry, film morphology, local electrochemical behavior and cytotoxic response of anodized AZ31B magnesium alloy. *J Mater Res Technol*. 2020;9:14754-70.
45. Chai L, Yu X, Yang Z, Wang Y, Okido M. Anodizing of magnesium alloy AZ31 in alkaline solutions with silicate under continuous sparking. *Corros Sci*. 2008;50:3274-9.
46. Qiu Z, Wang R, Zhang Y, Qu Y, Wu X. Study of coating growth behavior during the plasma electrolytic oxidation of magnesium alloy ZK60. *J Mater Eng Perform*. 2015;24:1483-91.
47. Yang S, Wang C, Li F, Liu N, Shi P, Wang B, et al. One-step in situ growth of a simple and efficient pore-sealing coating on micro-arc oxidized AZ31B magnesium alloy. *J Alloys Compd*. 2022;909:164710.

48. Fatimah S, Kamil MP, Han DI, Al-Zoubi W, Ko YG. Development of anti-corrosive coating on AZ31 Mg alloy subjected to plasma electrolytic oxidation at sub-zero temperature. *J Magnesium Alloys*. 2022;10(7):1915-29. <https://doi.org/10.1016/j.jma.2021.07.013>.
49. Wang Q, Tan L, Yang K. Preparation and in vitro degradation characterization of Si-containing coating on AZ31B alloy. *Mater Technol*. 2016;31:828-35.
50. Ardelean H, Frateur I, Zanna S, Atrens A, Marcus P. Corrosion protection of AZ91 magnesium alloy by anodizing in niobium and zirconium-containing electrolytes. *Corros Sci*. 2009;51:3030-8.
51. Zhao L, Cui C, Wang Q, Bu S. Growth characteristics and corrosion resistance of micro-arc oxidation coating on pure magnesium for biomedical applications. *Corros Sci*. 2010;52:2228-34.
52. Jian ZJ, Li M, Liu Q, Xu XC, Cheng Y, Zheng YF, et al. Micro-arc oxidization of a novel Mg-1Ca alloy in three alkaline KF electrolytes: corrosion resistance and cytotoxicity. *Appl Surf Sci*. 2014;292:1030-9.
53. Ningshen S, Sakairi M, Suzuki K, Ukai S. The corrosion resistance and passive film compositions of 12%Cr and 15%Cr oxide dispersion strengthened steels in nitric acid media. *Corros Sci*. 2014;78:322-34.
54. Chen L, Sheng Y, Zhou H, Li Z, Wang X, Li W. Influence of a MAO+PLGA coating on biocorrosion and stress corrosion cracking behavior of a magnesium alloy in a physiological environment. *Corros Sci*. 2019;148:134-43.
55. Srinivasan PB, Zettler R, Blawert C, Dietzel W. A study on the effect of plasma electrolytic oxidation on the stress corrosion cracking behaviour of a wrought AZ61 magnesium alloy and its friction stir weldment. *Mater Charact*. 2009;60:389-96.
56. Fang DR, Zhang ZF, Wu SD, Huang CX, Zhang H, Zhao NQ, et al. Effect of equal channel angular pressing on tensile properties and fracture modes of casting Al-Cu alloys. *Mater Sci Eng A*. 2006;426:305-13.
57. Törne K, Örnberg A, Weissenrider J. Influence of strain on the corrosion of magnesium alloys and zinc in physiological environments. *Acta Biomater*. 2017;48:541-50.

## Supplementary material

The following online material is available for this article:

Figure S1 – SEM micrographs (a) SE and (b) BSE mode of the SI-20 surface. EDS maps: c) Mg; d) Al; e) Si; f) Mn.

Figure S2 – SEM micrographs (a) SE and (b) BSE mode of the SI-30 surface. EDS maps: c) Mg; d) Al; e) Si; f) Mn.

Figure S3 – SEM micrographs (a) SE and (b) BSE mode of the PHO-20 surface. EDS maps: c) Mg; d) Al; e) Si; f) Mn.

Figure S4 – SEM micrographs (a) SE and (b) BSE mode of the PHO-30 surface. EDS maps: c) Mg; d) Al; e) Si; f) Mn.

Figure S5 – SEM micrographs (a) SE and (b) BSE mode of the BO-20 surface. EDS maps: c) Mg; d) Al; e) Si; f) Mn.

Figure S6 – SEM micrographs (a) SE and (b) BSE mode of the BO-30 surface. EDS maps: c) Mg; d) Al; e) Si; f) Mn.

Figure S7 – XPS Mg 1s high resolution spectra: a) SI-30; b) PHO-30; c) BO-30.

Figure S8 – XPS Si 2p high resolution spectra: a) SI-30; b) SI-20; c) BO-30.